AGU PUBLICATIONS

JGR

Journal of Geophysical Research: Planets

RESEARCH ARTICLE

10.1002/2016JE005040

Key Points:

- We extend an Earth-based H_2O snow model to simulate CO_2 snow albedo
- Improved CO_2 ice refractive indices produce very high (~0.96) CO_2 snow albedo
- We explore a range of conditions applicable to Mars and evaluate the model against measurements

Correspondence to:
D. Singh,
sdeepak@umich.edu

Citation:
Singh, D., and M. G. Flanner (2016), An improved carbon dioxide snow spectral albedo model: Application to Martian conditions, *J. Geophys. Res. Planets*, *121*, 2037–2054, doi:10.1002/2016JE005040.

Received 23 MAR 2016
Accepted 15 SEP 2016
Accepted article online 17 SEP 2016
Published online 9 OCT 2016

An improved carbon dioxide snow spectral albedo model: Application to Martian conditions

D. Singh[1] and M. G. Flanner[1]

[1]Climate and Space Sciences and Engineering, University of Michigan, Ann Arbor, Michigan, USA

Abstract Carbon dioxide ice is abundant on the Martian surface and plays an important role in the planet's energy budget due to its high reflectivity and seasonal variation. Here we adapt the terrestrial Snow, Ice, and Aerosol Radiation (SNICAR) model to simulate CO_2 snow albedo across the ultraviolet, visible, and near-IR spectra (0.2–5.0 μm). We apply recent laboratory-derived refractive indices of CO_2 ice, which produce higher broadband CO_2 snow albedo (0.93–0.98) than previously estimated. Compared with H_2O snow, we find that CO_2 snow albedo is much higher in the near-IR spectrum, less dependent on ice grain size, less dependent on solar zenith angle, and more susceptible to darkening from dust. A mass concentration of 0.01% Martian dust reduces visible and near-IR CO_2 snow albedos by about 60% and 35%, respectively. The presence of small amounts of H_2O snow on top of CO_2 snow can substantially decrease the surface albedo. Whereas 2.5 cm of H_2O snow can completely mask the impact of underlying CO_2 ice or the surface, roughly twice as much overlying CO_2 snow is required to mask underlying H_2O snow. Similarly, a 10% mixing ratio of H_2O ice embedded in CO_2 snow decreases broadband albedo by 0.18, while 10% CO_2 ice elevates H_2O snow broadband albedo by 0.10. We also present comparisons between hemispherical albedo produced by SNICAR and observations of directional reflectance of Martian polar ice caps. While imperfect, this best fit analysis provides general ranges of physical parameters in different Martian environments that produce reasonable model-observation agreement.

1. Introduction

The Martian atmosphere consists primarily of carbon dioxide, and Martian polar caps are covered primarily with carbon dioxide ice [*Leighton and Murray*, 1966; *Herr and Pimentel*, 1969; *Larson and Fink*, 1972; *Forget*, 1998; *Bibring et al.*, 2005]. H_2O ice is also present at the surface of the perennial ice caps, with small amounts of seasonal deposition in other parts of the planet [e.g., *Kieffer et al.*, 2000; *Bibring et al.*, 2004; *Brown et al.*, 2014]. Significant portions of atmospheric CO_2 (25–30%) deposit seasonally in each hemisphere, as indicated by model simulations and surface pressure measurements [*Tillman et al.*, 1993; *Forget et al.*, 1998; *Kieffer and Titus*, 2001]. To understand the impact of these ices on the planet's cryosphere albedo, it is important to accurately determine the spectral dependence of CO_2 snow albedo and influences of properties such as dust content, ice grain size, and snow thickness, as well as the albedo effects of mixing and layering of CO_2 and H_2O snow.

Our work determines the albedo of CO_2 snow by extending the Earth-based Snow, Ice, and Aerosol Radiation (SNICAR) model [*Flanner et al.*, 2007, 2009], originally designed for H_2O snow. SNICAR utilizes the multiple scattering, multilayer two-stream radiative approximation described by *Toon et al.* [1989], with the delta-hemispheric mean approximation. We extend the current version of SNICAR from 470 bands (over the wavelength range of 0.3–5.0 μm) to 480 bands spanning 0.2–5.0 μm at 10 nm spectral resolution. We include these extra 10 bands in the ultraviolet (UV) spectrum because of the lack of ozone in the Martian atmosphere compared to Earth [*Montmessin and Lefèvre*, 2013], meaning more UV radiation reaches the Martian surface and interacts with snow. A single-layer implementation of SNICAR can be operated interactively on the Web at: http://snow.engin.umich.edu.

Very few studies have focused on modeling of Martian CO_2 snow albedo across the UV, visible, and near-IR spectra [*Warren et al.*, 1990; *Hansen*, 1999; *Bonev et al.*, 2008]. *Langevin et al.* [2007] and *Appéré et al.* [2011] present modeled near-IR albedo of Martian cryospheric surfaces, as discussed in section 4. With the availability of more accurate and spectrally resolved laboratory measurements of CO_2 ice complex refractive indices across the solar spectrum [*Hansen*, 1997, 2005], we provide improved and updated spectral albedos of carbon dioxide snow with applicability to Martian conditions. The presence of light-absorbing impurities

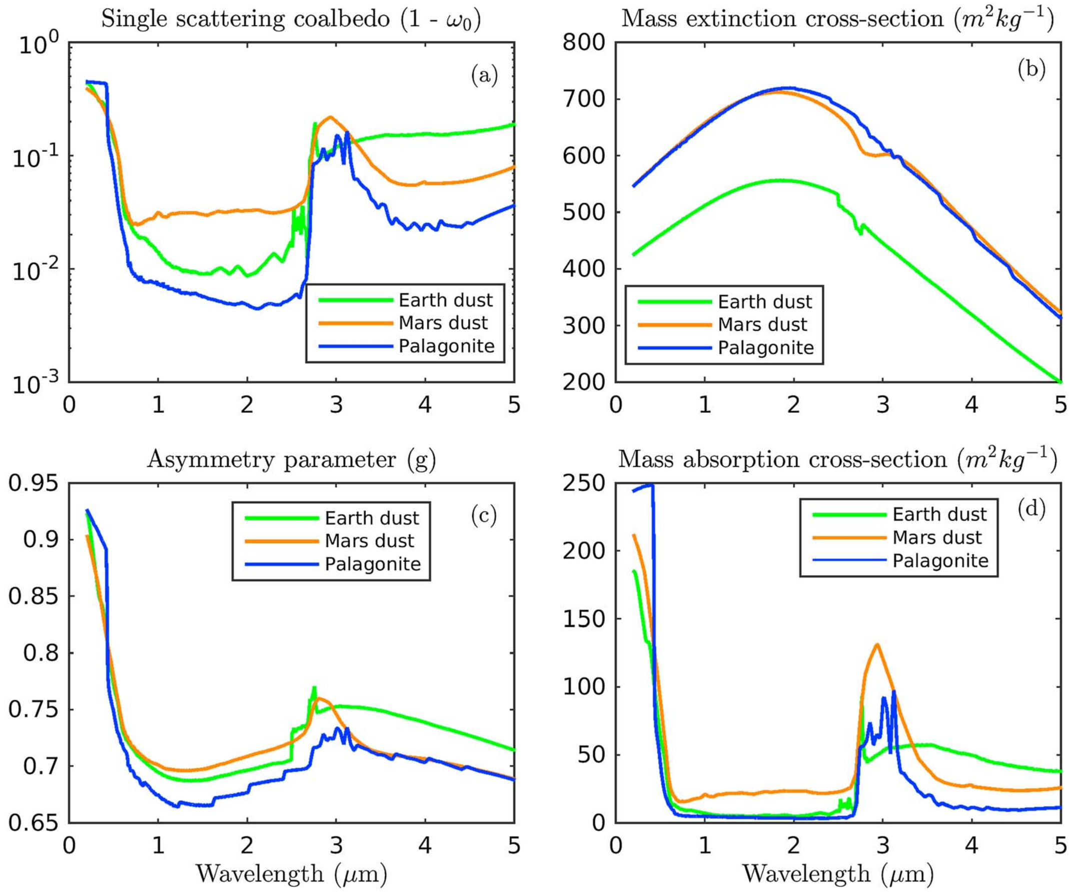

Figure 1. Spectral optical properties of the Earth dust, Martian dust, and palagonite applied in this study.

generally lowers snow albedo. We simulate the impact of Martian dust [*Wolff et al.*, 2006, 2009, 2010] and palagonite [*Clark et al.*, 1990; *Clancy et al.*, 1995] on surface cryosphere albedo. Palagonite is a volcanic rock and serves as a terrestrial analog for Martian dust [*Banin et al.*, 1997]. We perform multiple analyses to determine the sensitivity of cryosphere spectral albedo to the amount and type of dust, presence of both ices, ice grain size, snow layer thickness, and solar zenith angle. We also compare our simulations with observed Mars surface albedo derived from Compact Reconnaissance Imaging Spectrometer (CRISM) measurements and the Observatoire pour la Minéralogie, l'Eau, les Glaces et l'Activité (OMEGA) instrument [*Appéré et al.*, 2011] (section 4). Apparent albedos, derived by *Brown et al.* [2014] using CRISM measurements, were provided by Adrian Brown (SETI Institute, personal communication), and observations and modeled albedo from the OMEGA instrument were provided by Thomas Appéré (IPAG, Grenoble, personal communication).

2. Data and Methodology

Hansen [1997, 2005] made extensive laboratory measurements of the complex refractive indices of solid CO_2 ice in the spectral range from 0.174 μm to 333 μm. We apply these data along with Mie calculations to derive optical properties of different lognormal size distributions of CO_2 ice particles, reported with effective radius (r_{eff}), or the surface area-weighted mean radius of the size distribution. Our simulations of H_2O snow albedo utilize refractive indices of H_2O ice provided by *Warren and Brandt* [2008]. We use "central hematite" dust mineral fractions from *Balkanski et al.* [2007] as a proxy of typical Earth dust. These mineral abundances are representative of aeolian dust from the Saharan desert. Refractive indices for this dust mixture are derived by using the Maxwell-Garnett mixing approximation, following e.g., *Sokolik and Toon* [1999], along with measurements of mineral refractive indices from various sources. Refractive indices of Martian dust (hereafter Mars dust) were provided by Mike Wolff (Space Science Institute, personal communication) and were derived

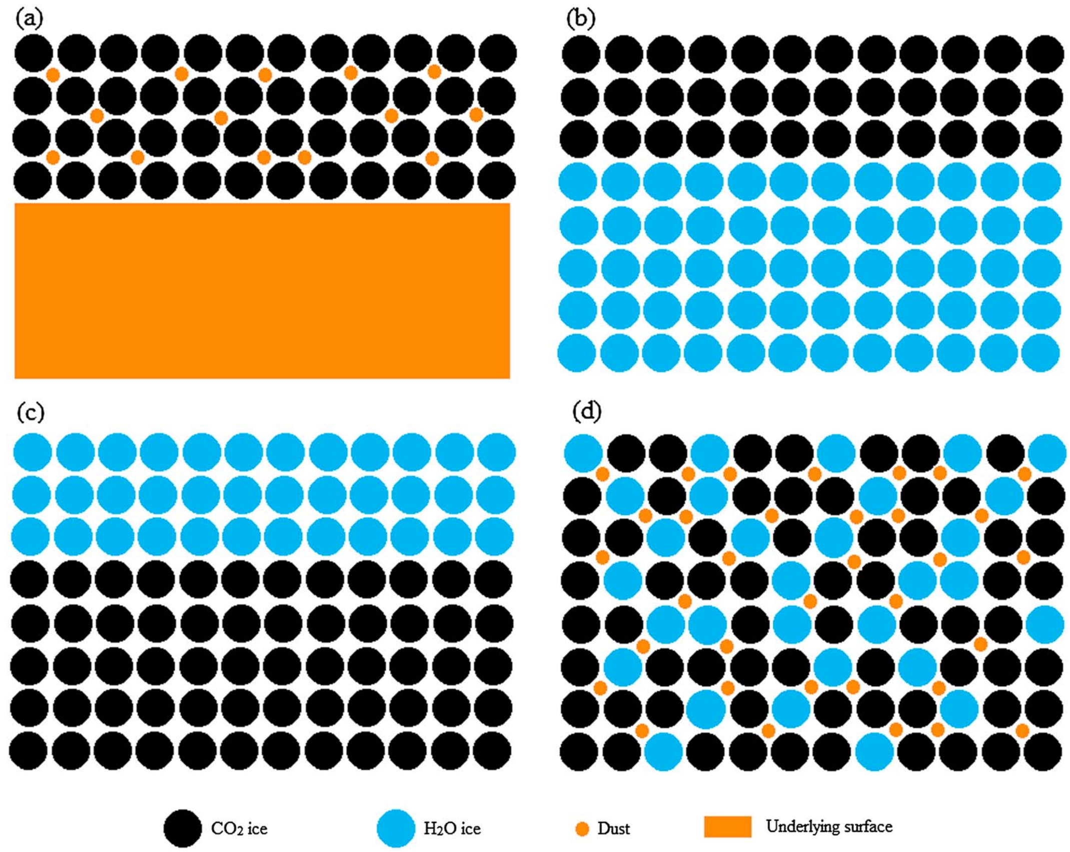

Figure 2. Schematic of the various model configurations applied in this paper: (a) a single CO_2 or H_2O snow layer (with dust) on top of solid underlying surface, (b) CO_2 snow with variable thickness on top of a semi-infinite H_2O snow layer, (c) H_2O snow with variable thickness on top of a semi-infinite CO_2 snow layer, and (d) mixed snow layers with dust.

by using data from instruments onboard the Mars Reconnaissance Orbiter, as described by *Wolff et al.* [2009], and *Wolff et al.* [2010]. We combine refractive indices of palagonite from *Clark et al.* [1990] over the 0.2 μm to 0.6 μm spectral range and measurements from 0.6 μm to 5 μm made by *Clancy et al.* [1995] to derive data over the solar spectrum. In this study, we divide our broadband (0.2–5.0 μm) into two subregions: visible (0.2–0.7 μm) and near-IR (0.7–5.0 μm).

We determine the spectrally varying single scatter albedo (ω_0), scattering asymmetry parameter (g), and mass extinction cross section for all three dust types by using Mie Theory with an assumed gamma size distribution [*Hansen and Travis*, 1974] with $r_{eff} = 1.5$ μm and effective variance ($\upsilon_{eff}) = 0.3$ [*Wolff et al.*, 2006]. Figure 1 shows the optical properties for these dust types. Mass absorption cross section (Figure 1d) is the product of single scatter coalbedo (Figure 1a) and mass extinction cross section (Figure 1b). We assume the same dust density of 2000 kg/m^3 for both palagonite and Mars dust [*Stroncik and Schmincke*, 2002], and a dust density of 2570 kg/m^3 for Earth dust, based on the volume fraction-weighted densities of the constituent minerals [*Balkanski et al.*, 2007].

The bulk optical properties (extinction optical depth (τ), ω_0, and g) for each snow layer are calculated from the abundances of each constituent [e.g., *Flanner et al.*, 2007], with τ calculated as the sum of that associated with each constituent, ω_0 as a τ-weighted average of each constituent, and g as a scattering optical depth (product of τ and ω_0) weighted average of the asymmetry parameter of each constituent. These bulk layer properties are then applied in the two-stream multiple scattering approximation adopted by SNICAR. We utilize this extended framework of SNICAR to first simulate the albedo of pure CO_2 snow across the visible and near-IR spectrum. We then explore and compare the impacts of Earth dust, Mars dust, and palagonite on CO_2 and H_2O snow albedo. Finally, we adopt a two-layer model (with the bottom layer being semi-infinite) to calculate the impacts of H_2O snow presence on top of CO_2 snow and vice versa. In all other cases we assume only a single snow layer, either with semi-infinite thickness or varying shallow thicknesses. Here a layer with

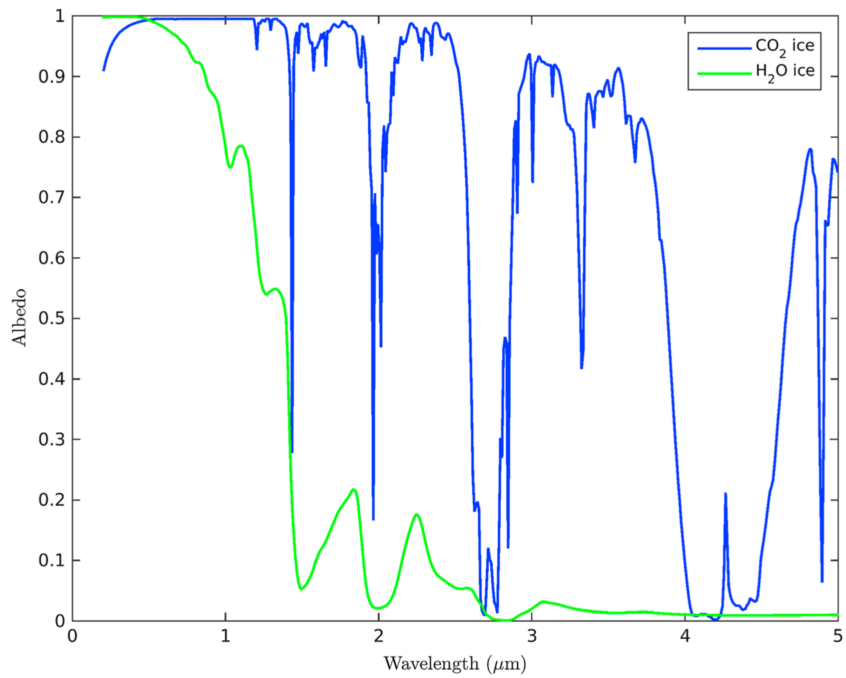

Figure 3. Comparison of CO_2 and H_2O snow spectral albedo simulated with the SNICAR model (grain size = 100 μm and solar zenith angle = 60°).

thickness of 100 m is referred to as semi-infinite. Figure 2 shows simplified diagrams of the various model configurations applied in this paper.

3. Results

Figure 3 shows the spectral hemispheric albedo of pure, semi-infinite CO_2 and H_2O snow with spherical grain effective radius of 100 μm and solar zenith angle of 60°. It is evident that the CO_2 is more reflective than H_2O snow, especially in the near-IR spectrum. Table 1 compares solar broadband, visible, and near-IR albedo for both types of snow, where band-averaged values are weighted with solar spectral irradiance measurements from *Labs and Neckel* [1968]. H_2O snow albedo is only about two-thirds of the CO_2 snow albedo in the near-IR spectrum, although this ratio is grain size-dependent (section 3.2). With the presence of both CO_2 and H_2O ices on Martian polar caps, the contrasting reflectivity of these types of snow could significantly impact planetary shortwave energy fluxes, both at the surface and top of atmosphere.

Snow albedo depends on many physical quantities, including grain size, solar zenith angle, layer thickness, and type and amount of impurities. We performed a sensitivity analysis to understand the effect of these parameters on carbon dioxide snow albedo and describe this analysis below. We assume an effective grain size of 100 μm and solar zenith angle of 60° for all analyses, unless stated otherwise. For comparing CO_2 and H_2O albedo, we also assume identical pore volume fractions for each type of ice. A typical bulk density of settled snow on Earth is 200 kg/m^3 (e.g., *EN 1991-1-3* [European Committee for Standardization, 2003]). Because the bulk densities of H_2O and CO_2 ice are assumed to be 917 kg/m^3 and 1500 kg/m^3, respectively, we therefore assume H_2O and CO_2 snow densities of 200 kg/m^3 and 327.15 (=200 × 1500/917) kg/m^3, respectively.

Table 1. Albedo Values for Pure, Semi-infinite CO_2 and H_2O Snow in Different Spectral Bands (Grain Size = 100 μm and Solar Zenith Angle = 60°)

	Pure CO_2	Pure H_2O
Visible (0.2–0.7 μm)	0.991	0.988
Near-IR (0.7–5.0 μm)	0.952	0.609
Broadband (0.2–5.0 μm)	0.970	0.787

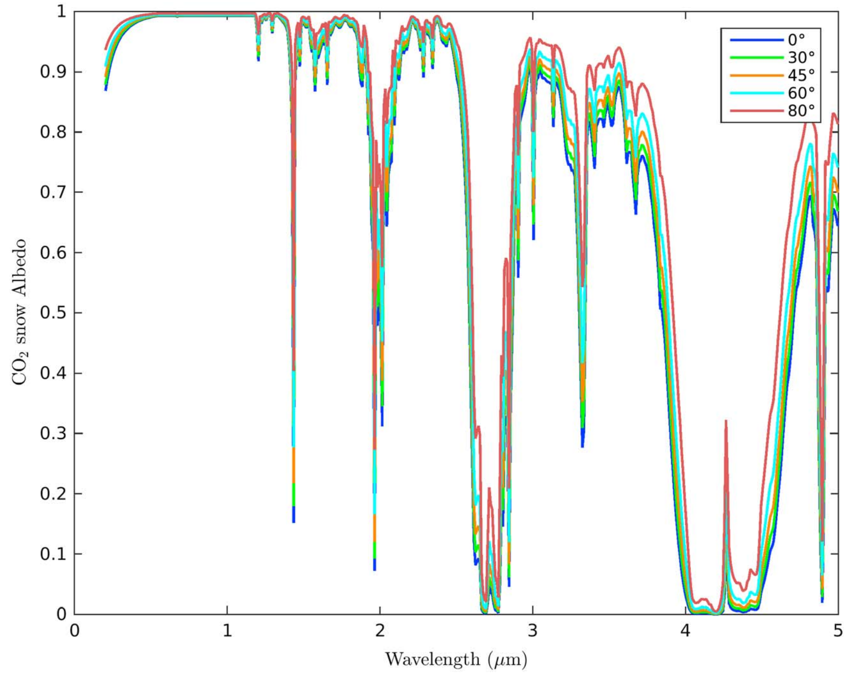

Figure 4. Variation of CO_2 snow albedo with solar zenith angle.

3.1. Solar Zenith Angle

We see little effect of solar zenith angle on CO_2 snow albedo (Figure 4). The broadband albedo only changes from 0.98 to 0.96 over the 80° change in zenith angle. This compares with H_2O snow albedo, which varies from 0.75 to 0.82 for the same set of parameters. Variability in albedo with solar zenith angle is greater in more absorptive parts of the spectrum (i.e., the near-IR), but for CO_2 snow the variability is small in the parts of the spectrum containing most of the solar energy.

3.2. Grain Size

We simulate a monotonic decrease in snow albedo with increasing effective grain size (Figure 5). With larger grain size, ice volume per surface area increases, resulting in greater absorption of light, as also occurs with H_2O snow [e.g., *Wiscombe and Warren*, 1980]. The broadband (near-IR) albedo of CO_2 snow drops from 0.98 to 0.93 (0.96 to 0.89) for grain size increasing from 50 μm to 1500 μm. This is also smaller variability than exhibited by H_2O snow, whose broadband (near-IR) albedo changes from 0.82 to 0.65 (0.66 to 0.37) over the same range in effective grain size. CO_2 snow albedo varies less with grain size because CO_2 ice is inherently less absorptive in the near-IR than H_2O ice. Consequently, the incremental increase in absorption associated with increasing photon path length within larger ice grains is smaller for CO_2 snow than H_2O snow.

3.3. Snow Thickness

Figure 6 shows the combined impacts of snow thickness and grain size on CO_2 and H_2O broadband snow albedo, for snow overlying a surface with spectrally constant albedo of 0.2 (model configuration shown in Figure 2a). For a given grain size, CO_2 snow albedo has a larger variation over the entire thickness range compared to H_2O snow albedo. CO_2 snow albedo is almost independent of grain size when the snow layer is thick, and consequently, all curves saturate at a similarly high albedo ranging from 0.93 to 0.98. However, H_2O snow albedo has greater dependence on grain size, as each curve saturates at a different albedo ranging from 0.65 to 0.82.

We define “saturation thickness” as the snow thickness needed for the broadband albedo to differ by less than 0.01 from its semi-infinite value. Once the snow layer thickness exceeds the saturation thickness, the impact of the underlying surface becomes negligible as an insignificant amount of light penetrates through the snow to interact with the underlying surface. We note, however, that the penetration depth of radiation in

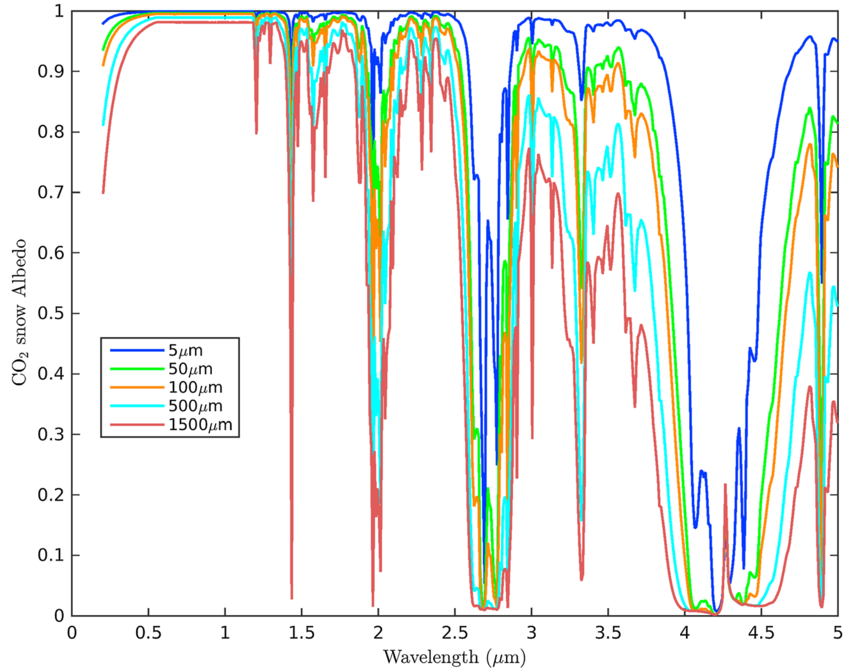

Figure 5. Variation of CO_2 snow albedo with effective grain radius.

snow depends strongly on wavelength, with multiple scattering leading to much deeper penetration and influence of underlying substrate at wavelengths where the ice absorbs weakly [e.g., *Wiscombe and Warren*, 1980]. The saturation thickness also depends on snow density, with higher density producing lower saturation thickness. Table 2 presents the saturation thickness required for different grain sizes for both types

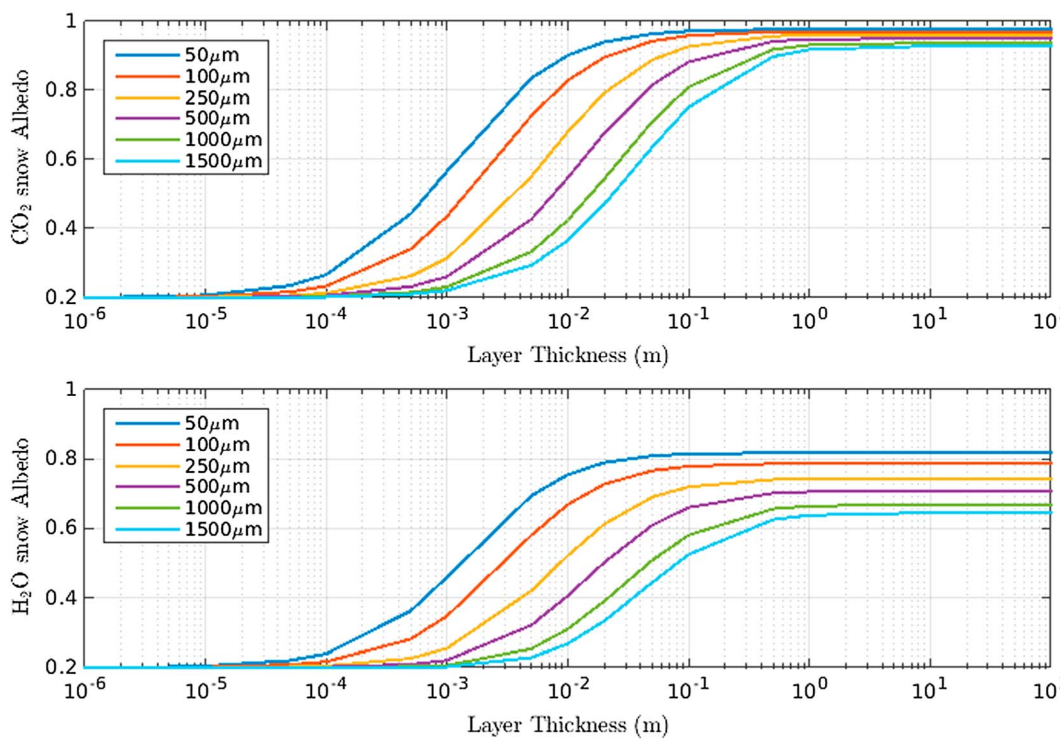

Figure 6. Broadband (top) CO_2 and (bottom) H_2O snow albedo dependence on snow layer thickness for various effective grain sizes. The underlying surface is assumed to have a constant albedo of 0.2. The snow density is 327.15 kg/m^3 and 200 kg/m^3 for CO_2 and H_2O snows, respectively.

Table 2. Saturation Snow Layer Thickness With Various Grain Sizes for Each Type of Snow[a]

Grain Size	CO_2 Snow Saturation Thickness	H_2O Snow Saturation Thickness
50 μm	6.5 cm	5.0 cm
100 μm	10.9 cm	8.9 cm
250 μm	24.0 cm	18.8 cm
500 μm	43.1 cm	33.7 cm
1000 μm	73.8 cm	59.4 cm
1500 μm	100.2 cm	83.2 cm

[a] CO_2 and H_2O snow densities are 327.15 and 200 kg/m^3, respectively.

of snow. The saturation thickness is grain size-dependent, increasing from about 6 to 100 cm, and from about 5 to 83 cm as grain size increases from 50 to 1500 μm for CO_2 and H_2O snow, respectively. With other factors equal, CO_2 snow has higher saturation thickness than H_2O snow because CO_2 ice is less absorptive than H_2O ice, especially in the near-IR region, enabling multiple scattered photons to penetrate deeper in the snow. Also, the difference in saturation thicknesses increases with larger grain size because of less dependency of CO_2 snow albedo on grain size compared to H_2O snow (section 3.2). Finally, we note that studies on optical properties of ice particles have found that the scattering asymmetry parameter is generally smaller for nonspherical ice particles than equal volume/area ice spheres [e.g., *Fu*, 2007; *Libois et al.*, 2013; *Räisänen et al.*, 2015]. An implication of this is that saturation thickness will be smaller for nonspherical ice particles than values reported here, as photons are scattered less preferentially into the forward direction.

3.4. Dust Type

The snow albedo impacts of different types of dust depend on their optical properties and in particular on their mass absorption cross section. Here we compare the impacts of Earth dust, Mars dust, and palagonite on semi-infinite snow albedo (Figure 7). Again, identical size distributions are assumed for each type of dust, and only the refractive indices are varied as input to Mie calculations. Mars dust has the greatest albedo impact of the three between wavelengths of 0.5 and 2.5 μm, which contains most of the incident solar energy, while palagonite has the least. Mars dust is relatively dark due to the presence of higher amount of iron oxides [*Bell et al.*, 1990; *Bell*, 1996; *Christensen et al.*, 2000, 2001a, 2001b], combined with its large mass

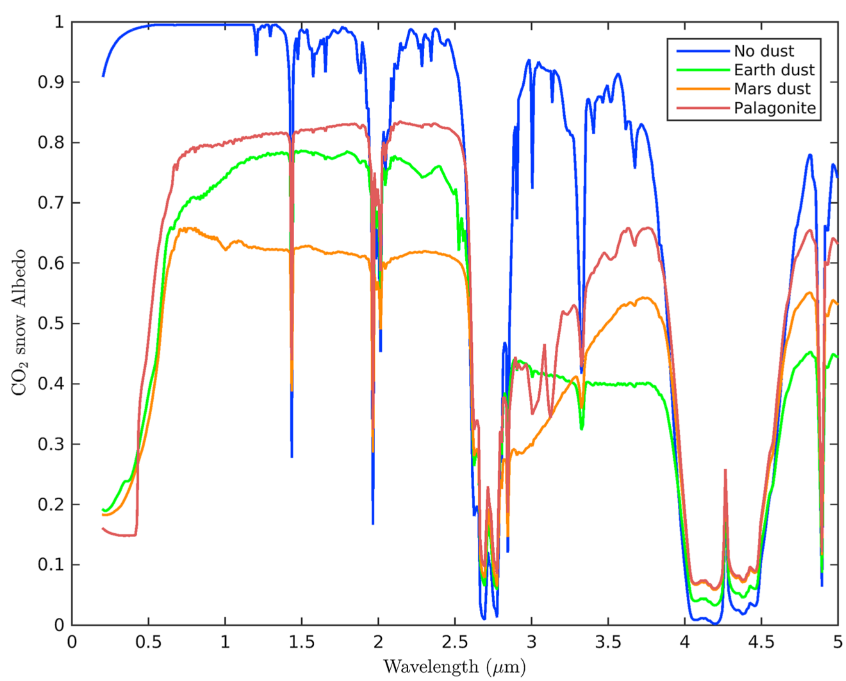

Figure 7. Impact of different types of dust on CO_2 snow albedo, with dust mass mixing ratio of 0.01%. The assumed snow grain size is 100 μm.

Table 3. Impact of Different Types of Dust on CO_2 Broadband Snow Albedo (Grain Size of 100 μm), With Dust Mass Mixing Ratio of 0.01%

	Pure CO_2	Earth Dust	Mars Dust	Palagonite
Visible (0.2–0.7 μm)	0.991	0.429	0.395	0.477
Near-IR (0.7–5.0 μm)	0.952	0.718	0.616	0.779
Broadband (0.2–5.0 μm)	0.970	0.583	0.513	0.637

extinction cross section. Although average Earth dust has a lower near-IR single-scatter albedo than the Mars dust, it also has a lower mass extinction cross section across the spectrum, due to its larger density, leading to lower absorption per unit mass of dust, expressed via the mass absorption cross section (Figure 1d).

We consider "mass mixing ratio" as the mass of impurity divided by the mass of ice in which the impurity is mixed. Table 3 presents the effective CO_2 snow albedo in the presence of 0.01% mass mixing ratio of dust (kilogram of dust/kilogram of ice). Dust causes a larger albedo drop in the visible region (~0.6) compared to the near-IR region (~0.3) because all three types of dust have very low single scatter albedo in the blue and green spectra, while ice grains scatter very efficiently at these wavelengths (Figure 1). Furthermore, the drop in albedo in the blue spectrum (~0.8) is much higher than the drop in the red spectrum (~0.3), helping explain the planet's red appearance even in its cryospheric regions. Although palagonite is less absorptive than Mars dust, the spectral variations in albedo impacts of the two species are similar.

Table 4 presents the effective H_2O snow albedo in the presence of 0.01% mass mixing ratio of dust. Pure H_2O snow is relatively absorptive in the near-IR spectral region (Tables 1 and 4), so dust has little impact on near-IR albedo, or in the most absorptive portions of the spectrum, it even increases albedo (Figure 8). Fundamentally, this occurs because the single-scatter albedo of dust exceeds that of H_2O ice grains at wavelengths longer than about 1.5 μm. Similar to CO_2 snow, the drop in albedo is large in the visible region for H_2O snow. However, in the near-IR region the change is less than 0.1, leading to smaller broadband albedo impacts of dust on H_2O snow albedo than on CO_2 snow albedo. These differences indicate that dust can have greater impact on Martian cryosphere albedo than Earth cryosphere albedo due to the higher abundance of CO_2 ice compared to H_2O ice.

3.5. Dust Concentration

Figure 9 shows the effect of varying amounts of Mars dust on CO_2 snow albedo (Figure 2a). It is obvious that albedo decreases with increasing amount of dust, except in the strong absorption bands of CO_2 ice (e.g., near 1.4 μm, 1.9 μm, and 2.7 μm). Again, we see maximum impact in the visible part of the spectrum. Saturation of the albedo from this type of dust is evident with dust mixing ratios exceeding 0.01%, with almost no difference in albedo between scenarios with 0.1% and 1% dust. Also, the strong absorption features of CO_2 snow at various wavelengths disappear with high dust concentrations.

3.6. Presence of Both H_2O and CO_2 Ice

3.6.1. Separate Layers

H_2O and CO_2 ice interact quite differently with radiation in the visible and near-IR portions of the spectrum and also exhibit different sensitivities to different physical parameters. These ice types are also known to coexist on the surface of Mars [e.g., *Byrne et al.*, 2008; *Brown et al.*, 2014]. Here we explore the albedo effects associated with thin slabs of one type of ice overlying the other, building on sensitivity studies conducted by *Warren et al.* [1990]. Figure 10 shows the spectral albedo of surfaces with H_2O snow on top of CO_2 snow (scenario shown in Figure 2c), and Figure 11 shows the albedo with the reverse situation (scenario shown in Figure 2b).

Table 4. Impact of Different Types of Dust on H_2O Broadband Snow Albedo (Grain Size of 100 μm), With Dust Mass Mixing Ratio of 0.01%

	Pure H_2O	Earth Dust	Mars Dust	Palagonite
Visible (0.2–0.7 μm)	0.988	0.450	0.415	0.494
Near-IR (0.7–5.0 μm)	0.609	0.551	0.503	0.599
Broadband (0.2–5.0 μm)	0.787	0.504	0.461	0.550

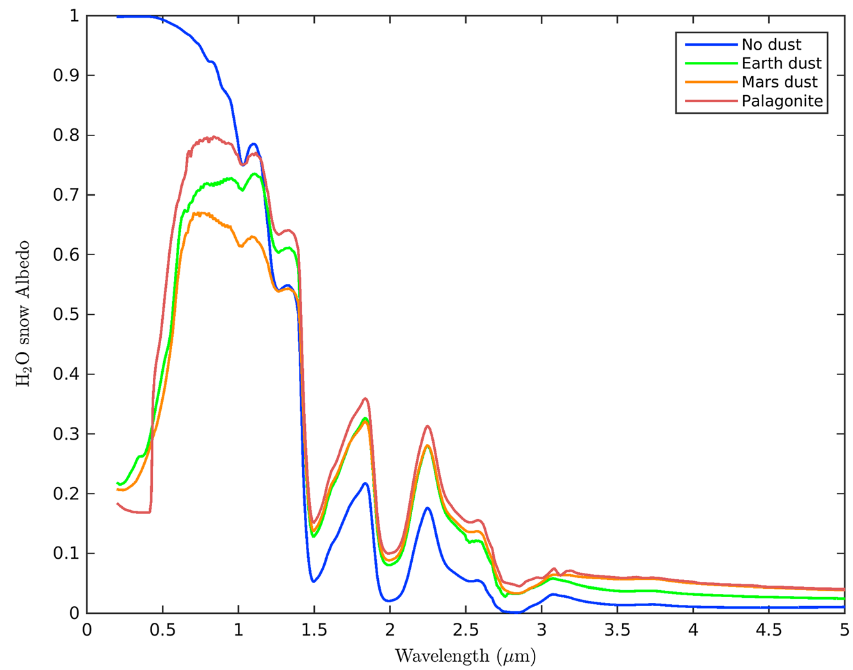

Figure 8. Impact of different types of dust on H_2O snow albedo, with dust mass mixing ratio of 0.01%. The assumed snow grain size is 100 μm.

Albedo decreases markedly with the presence of thin slabs of H_2O snow on top of CO_2 snow. This decrease occurs more rapidly with increasing thickness of H_2O ice than the rate of albedo increase that occurs with increasing thickness of CO_2 snow overlying H_2O snow. For a grain size of 100 μm, about 2.5 cm of H_2O snow is required to completely mask out the albedo effect of CO_2 snow (Table 5), whereas about 5.5 cm of CO_2 snow is required to completely mask out the albedo effect of underlying H_2O snow (Table 6). Again, differences are more pronounced in the near-IR spectrum (Figure 3 and Table 1), where the contrast in

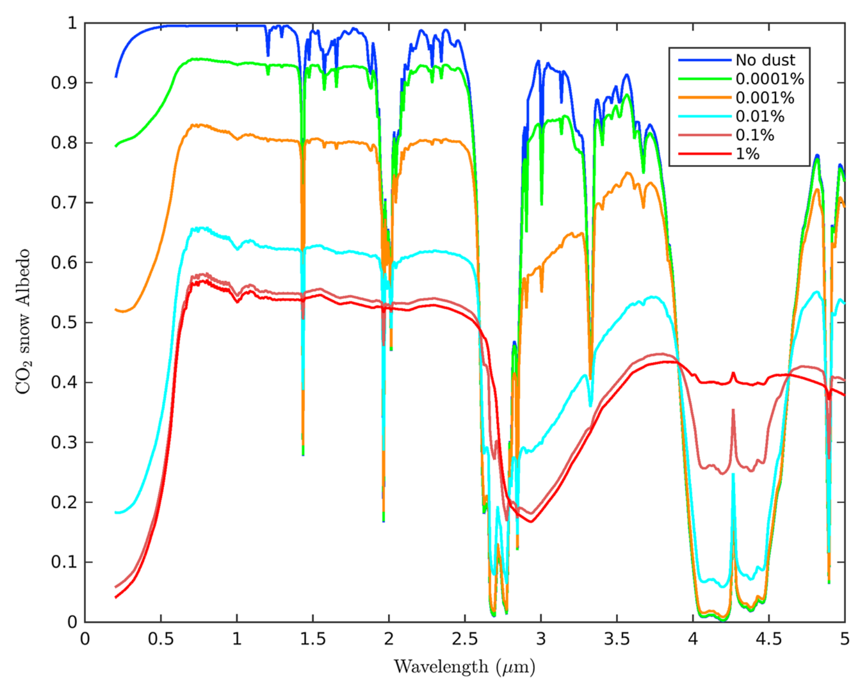

Figure 9. Impact of various amounts of Martian dust on CO_2 snow albedo. Snow effective grain radius is 100 μm.

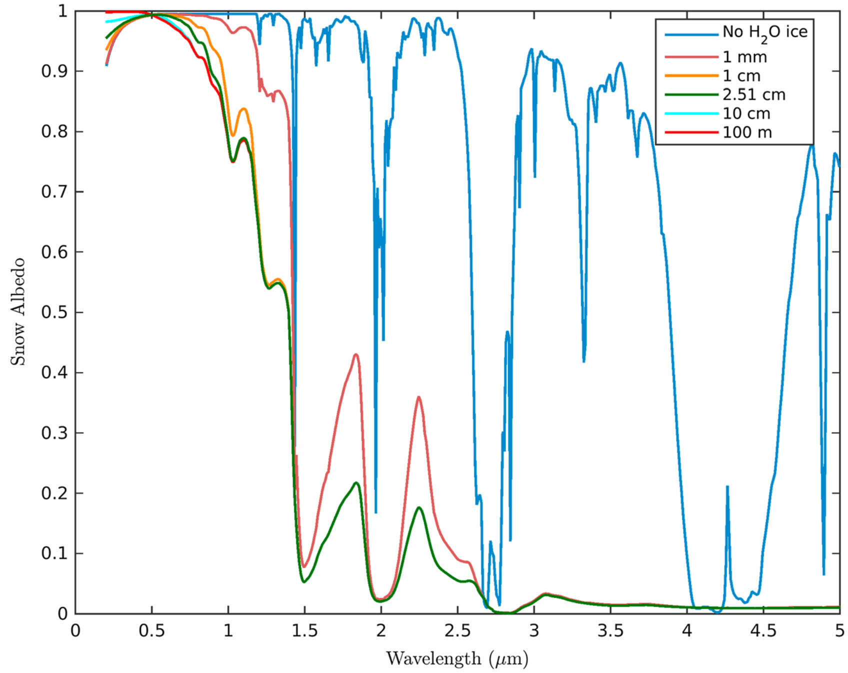

Figure 10. Spectral albedo of surfaces with H_2O snow layers of varying thickness on top of CO_2 snow. The green curve thickness corresponds to saturation thickness.

absorptivity between CO_2 and H_2O ice is greater (Tables 5 and 6). Marked rows in Tables 5 and 6 correspond to saturation thickness. In summary, very little H_2O snow is needed to mask the presence of underlying CO_2 snow, whereas a larger thickness of CO_2 snow is needed to prevent underlying, more absorptive H_2O snow from effecting surface albedo.

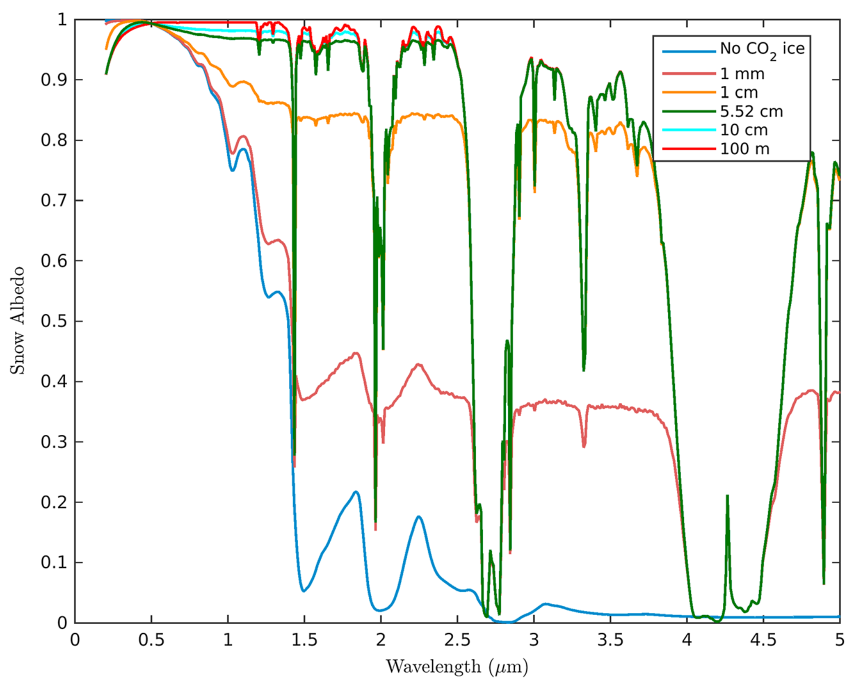

Figure 11. Spectral albedo of surfaces with CO_2 snow layers of varying thickness on top of H_2O snow. The green curve thickness corresponds to saturation thickness.

Table 5. Broadband Albedos of Surfaces With H_2O Snow Layers on Top of CO_2 Snow

H_2O Layer Thickness	Vis	Near-IR	Broadband
0	0.991	0.952	0.970
1 mm	0.991	0.739	0.857
1 cm	0.991	0.639	0.804
2.51 cm[a]	0.987	0.618	0.793
10 cm	0.990	0.610	0.787
100 m	0.988	0.609	0.787

[a]Saturation thickness (section 3.3).

Warren et al. [1990] determined that the presence of H_2O snow on top of CO_2 snow will increase the net surface albedo, contrary to the analysis presented here. The CO_2 ice refractive indices applied in that study, however, were measured by using unpurified commercial dry ice [*Egan and Spagnolo*, 1969], and data in the 1.0–2.5 μm spectral region were extrapolated from the 0.3–1.0 μm spectral region. The higher-quality measurements on pure CO_2 ice provided by *Hansen* [1997, 2005], and applied here, indicate that CO_2 ice is much less absorptive than previously assumed, leading to our opposite conclusion.

Figure 12 shows the broadband net surface albedo dependence on layer thickness for different snow types. The black lines indicate the saturation thickness (section 3.3) for the two scenarios discussed above. To further explore the behavior of albedo with layer thickness, we divide each curve into two regions: with thickness lesser and higher than saturation thickness. Table 7 lists the slopes of albedo per layer thickness for these two regions. For top layer thickness less than saturation thickness (first region), higher slope (in absolute values) of data shown in Figure 12a than Figure 12b substantiates the conclusion that H_2O snow is harder to mask out compared to CO_2 snow. However, for the second region with thickness higher than saturation thickness, the scenario with overlying CO_2 snow (Figure 12b) demonstrates higher absolute slope than the reverse situation. This indicates that H_2O snow is less sensitive to thickness variation (once a minimum threshold is reached), owing to its more absorptive nature in the near-IR spectrum compared to CO_2 snow.

3.6.2. Mixed Layers

In addition to the possibility of different snow types being present as separate layers, both types of snow can also become mixed together on the surface of Mars [e.g., *Brown et al.*, 2014]. In this section, we explore the net surface albedo changes caused by one snow type becoming mixed with the other snow type. In practice, this is simulated by treating the less abundant ice type as an externally mixed “impurity” with specified mass mixing ratio (scenario shown in Figure 2d), analogous to the treatment of dust described earlier. Figure 13 shows the net surface albedo when H_2O snow is present as an impurity within CO_2 snow, and Figure 14 shows the net surface albedo for the reverse situation. We assume a semi-infinite snow layer and effective grain size of 100 μm for both snowpacks.

Broadband (near-IR) albedo drops by ~0.18 (~0.34) for an associated increase of H_2O snow from 0% to 10% within CO_2 snow. However, broadband (near-IR) albedo increases by ~0.10 (~0.18) in the reverse situation. This is consistent with our earlier findings that H_2O snow is relatively darker (especially in the near-IR region) compared to CO_2 snow, hence causing larger impact on net surface albedo. The 0.01% of H_2O snow is sufficient to reduce the net broadband albedo of the mixture by 0.03, while 1% of CO_2 snow is required to increase the net surface broadband albedo of the mixture by same amount.

Table 6. Broadband Albedos of Surfaces With CO_2 Snow Layers on Top of H_2O Snow

CO_2 Layer Thickness	Vis	Near-IR	Broadband
0	0.988	0.609	0.787
1 mm	0.988	0.703	0.837
1 cm	0.989	0.869	0.925
5.52 cm[a]	0.989	0.934	0.960
10 cm	0.990	0.943	0.965
100 m	0.991	0.952	0.970

[a]Saturation thickness (section 3.3).

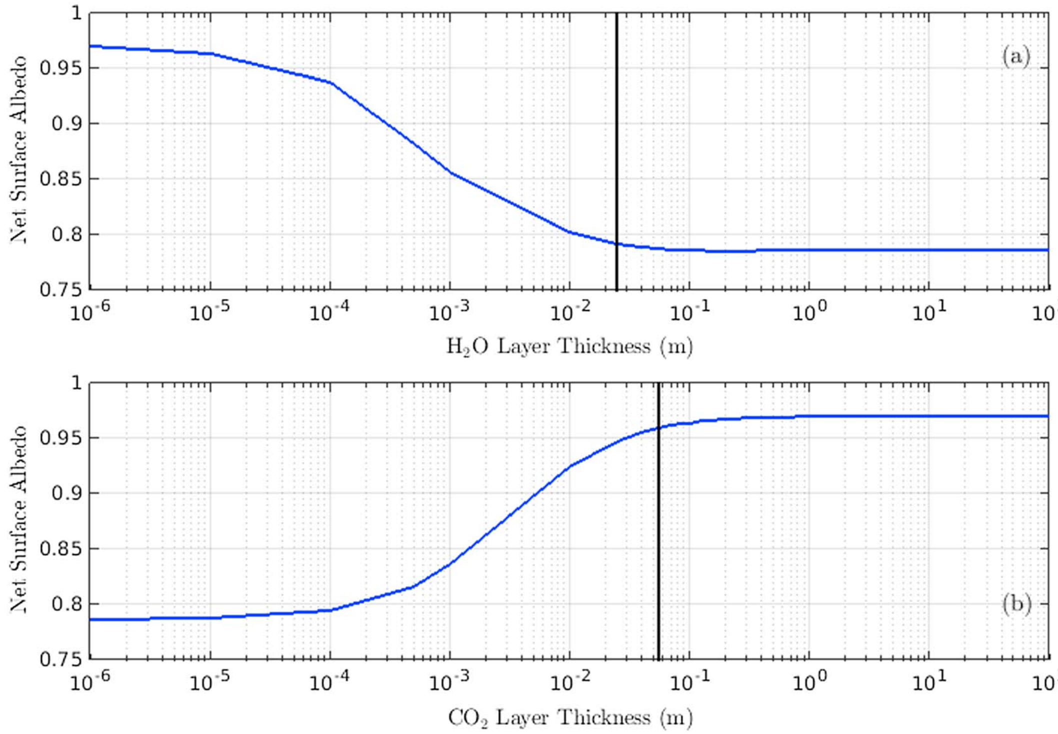

Figure 12. Dependence of net surface broadband snow albedo on layer thickness for (a) an H_2O snow layer on top of a semi-infinite CO_2 snow layer and (b) a CO_2 snow layer on top of a semi-infinite H_2O snow layer. The black line indicates the saturation thickness for each case. Snow grain size is assumed to be 100 μm in both cases.

4. Comparison With Observed Martian Albedo

In this section, we compare our simulations with some observations of surface reflectance in the Martian cryosphere and try to identify parameter combinations that produce reasonable agreement between the modeled and observed data. We first note that SNICAR produces directional-hemispherical albedo, whereas the CRISM and OMEGA observations evaluated here are bidirectional reflectances. This discrepancy renders the model-observation comparison imperfect, but the analysis does have some usefulness in illustrating broad agreement between modeled and observed spectral reflectance features and in identifying general ranges of physical parameters that produce reasonable modeled spectra in different environments.

4.1. Comparison With CRISM Measurements

We obtained spectral reflectance data for one location in the Southern Hemisphere (point A, Figure 3 of *Brown et al.* [2014]) identified to have a majority of CO_2 ice (hereafter location S), and one location from the Northern Hemisphere (point B, Figure 4c of *Brown et al.* [2012]) identified to have mostly H_2O ice (hereafter location N). The observed reflectance were obtained by using radiance measurements from CRISM in the 1–4 μm spectral range. Therefore, we only compare our simulations in this spectral range.

Since the reflectance data display a time dependency, we choose two of the least noisy end-member (i.e., most different) observed spectra for each location. Then we determine the best fit for each location by minimizing the weighted root-mean-square error (RMSE) between each of the identified spectral reflectance curves and our hemispheric albedo simulations, which span a wide range of the parameter space described

Table 7. Slopes of Albedo per Change in Layer Thickness for the Two Scenarios Shown in Figure 12

Thickness Regime	H_2O Snow Layer on Top of CO_2 Snow Layer (Figure 11a)	CO_2 Snow Layer on Top of H_2O Snow Layer (Figure 11b)
Less than saturation thickness	$-7.10\ m^{-1}$	$+3.14\ m^{-1}$
Higher than saturation thickness	$-5.54 \times 10^{-5}\ m^{-1}$	$+1.05 \times 10^{-4}\ m^{-1}$

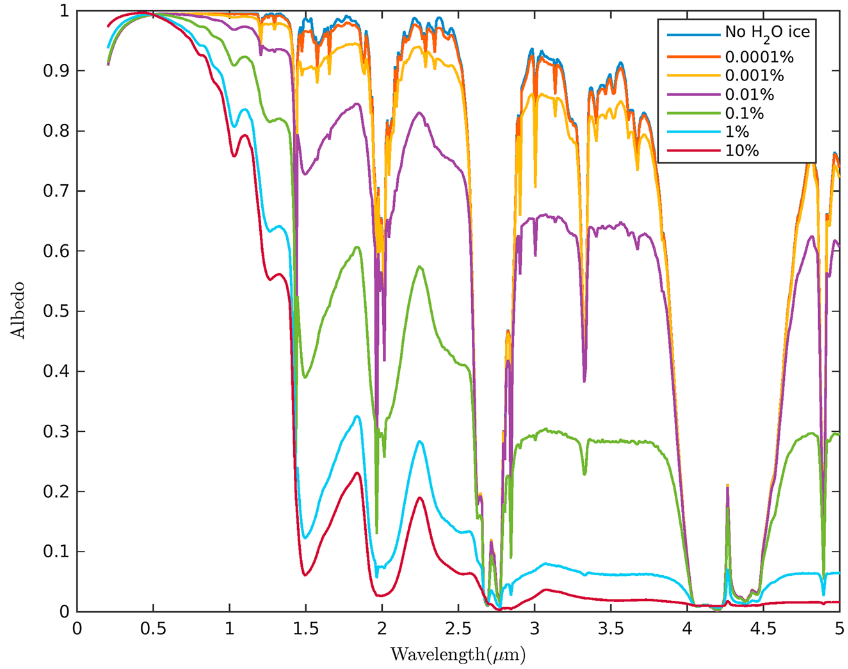

Figure 13. Spectral albedo of surfaces with H_2O ice present as an impurity within CO_2 snow. Effective grain size for both snow types is 100 μm, and the layer is semi-infinite.

earlier. Spectral weighting for the RMSE calculation is done with the same solar spectral irradiance measurements [*Labs and Neckel*, 1968] applied throughout this study. Therefore, reflectance values for longer wavelengths are weighted less strongly and consequently do not fit as well with observations. We also note that reflectance measurements at wavelengths longer than 2.5 μm are not very reliable (on Earth too) because there is very little incoming solar energy at these wavelengths.

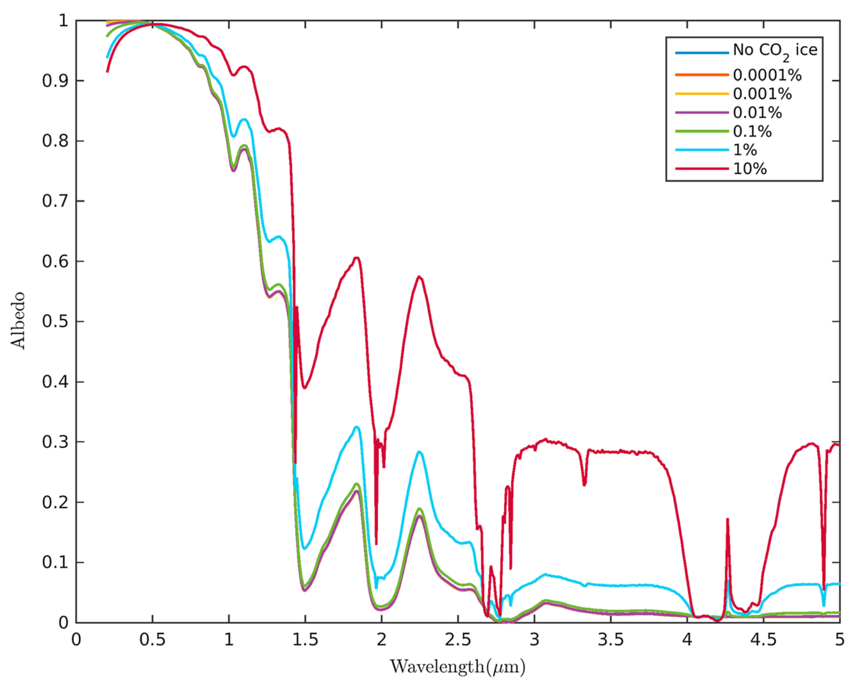

Figure 14. Spectral albedo of surfaces with CO_2 ice present as an impurity within H_2O snow. Effective grain size for both snow types is 100 μm, and the layer is semi-infinite.

Table 8. Best Fit Parameter Combinations for Each Mars Location[a]

Location S			Location N		
	$L_s = 276$	$L_s = 337$		$L_s = 13$	$L_s = 65$
CO_2 ice grain size	1000 μm	3000 μm	H_2O ice grain size	100 μm	500 μm
H_2O ice grain size	100 μm	200 μm	CO_2 ice grain size	na	na
Amount of H_2O ice	0.024%	0.07%	Amount of CO_2 ice	na	na
Amount of dust	0.0042%	0.003%	Amount of dust	0.06%	0.01%
RMSE (solar weighted)	0.06	0.07	RMSE	0.055	0.057

[a]The H_2O ice at location S is simulated as a mixture within the CO_2 snow, as opposed to a distinct layer. The term na denotes not available.

Table 8 lists the best fit values of various parameters along with spectrally weighted RMSE values for both locations. The presence of any CO_2 ice tends to increase the RMSE at location N. This happens because observations from location N occurred during early spring to midsummer in that hemisphere, when there is likely no CO_2 ice present on the surface [e.g., *Brown et al.*, 2014]. Location S needs about an order of magnitude less dust amount as compared to location N for optimal fitting. One reason for this is that location S is deemed to have some coincident H_2O ice, which functions as a competing impurity to dust because H_2O snow substantially darkens albedo in the near-IR spectral region. For location S, changing CO_2 ice grain size does not have any significant impact on RMSE, while the H_2O ice grain size has significant impact on RMSE for location N. This is consistent with our results described in section 3.2.

Figures 15 and 16 show the observed spectral reflectance curves along with simulated albedos by using parameter values shown in Table 8. We observe an outlier point at 2.7 μm wavelength in the observed data for both locations and at all times. Reflectance values at this wavelength are uncharacteristically higher than at nearby wavelengths, whereas both CO_2 and H_2O snows have very high absorptivity at this wavelength (Figure 3). This leads us to suggest that the high observed reflectance at this wavelength is spurious and may be due either to an artefact of the measuring spectrometer (CRISM), atmospheric anomalies associated with dust or clouds [*Brown et al.*, 2010], and/or a calibration issue in the retrieval of surface reflectance at that

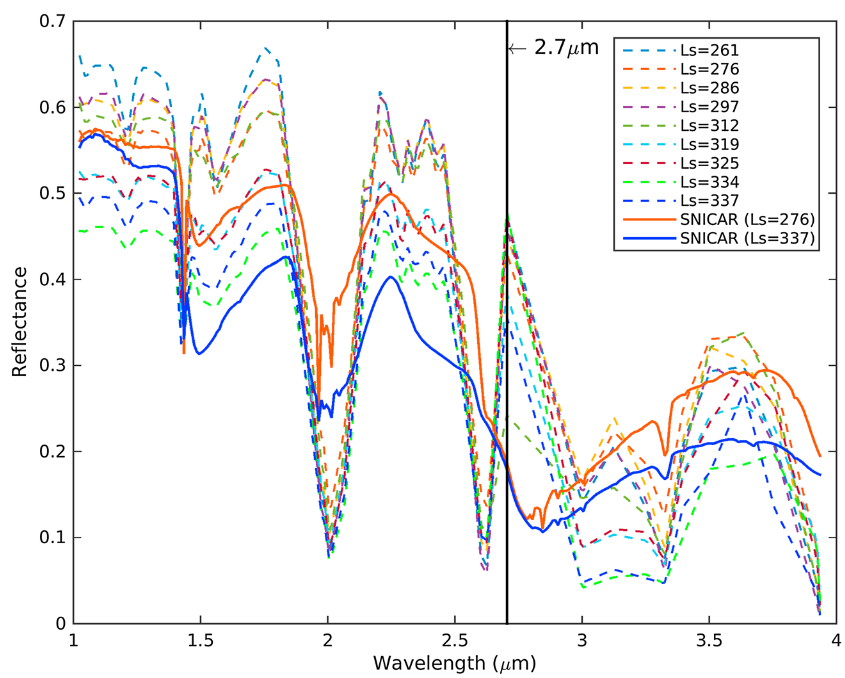

Figure 15. Observed reflectance for location S (dotted curves) along with modeled albedo using best fit parameters (solid blue curve). The black vertical line at 2.7 μm indicates the outlier described in the text.

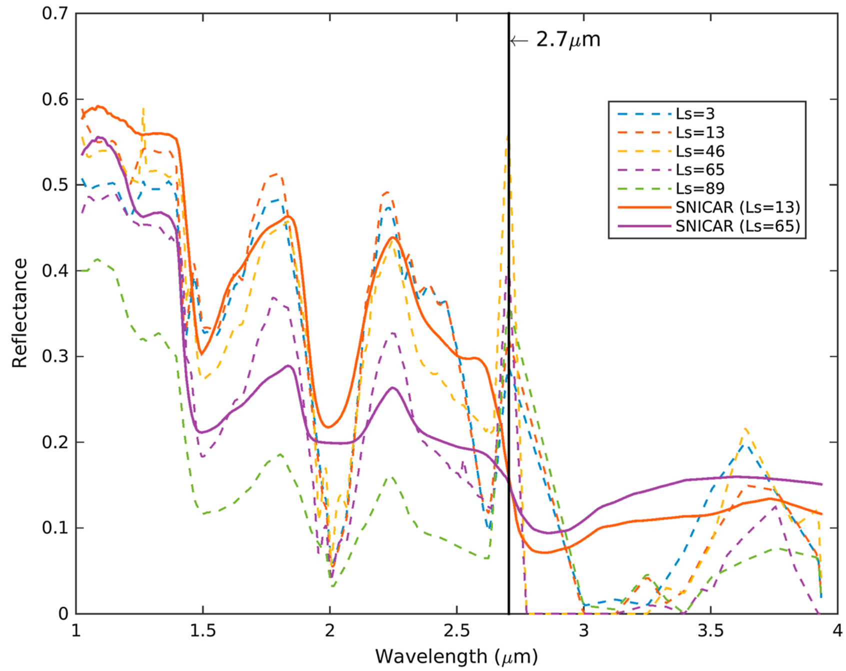

Figure 16. Same as Figure 15 but for location N.

wavelength. We also emphasize again that the low intensity of sunlight at this wavelength renders the reflectance measurements less certain than at shorter wavelengths.

4.2. Comparison With OMEGA Measurements

We also obtained spectral reflectance for Observation 2621_1 from the OMEGA instrument (see Figure 18 from *Appéré et al.* [2011]; shown later here) and modeled spectral reflectance of snow mixture simulated with a different radiative transfer model developed by *Douté and Schmitt* [1998].

As shown in Table 9 and Figure 17, *Appéré et al.* [2011] achieved good agreement between simulated near-IR snow reflectance and OMEGA observations of a CO_2-rich deposit by assuming a mixed CO_2/H_2O snow configuration with a CO_2 grain size of 7 cm, which interestingly is much larger than what is deemed to be realistic under most conditions [*Barr and Milkovich*, 2008]. We also achieved a reasonable fit (spectrally weighted RMSE of 0.027) against the OMEGA observations presented by *Appéré et al.* [2011] with a mixed CO_2 and H_2O configuration of SNICAR applying a smaller CO_2 grain radius and slightly different mass fractions of dust and H_2O (Table 9 and Figure 17), though admittedly the fit is not quite as good as that obtained by *Appéré et al.* [2011]. It is plausible that the better agreement obtained by *Appéré et al.* [2011] is due to their use of a directional reflectance radiative transfer model [*Douté and Schmitt*, 1998], which provides a more consistent comparison with the measurements. Uncertainties in the observations, however, are described by *Appéré et al.* [2011] to be roughly 20%, indicating that both sets of modeled spectra are within the range of uncertainty. Finally, we note that the quality of our fit ceases to change much with larger grain sizes of CO_2 ice.

Table 9. Comparison of Best Fit Parameters Between SNICAR and *Appéré et al.* [2011]

	SNICAR	*Appéré et al.* [2011]
CO_2 ice grain size	3000 μm	7 cm
Amount of CO2 ice	99.83%	99.75%
H_2O ice grain size	100 μm	200 μm
Amount of H_2O ice	0.16%	0.19%
Dust grain size	1.5 μm	13 μm
Amount of dust	0.0094%	0.06%
RMSE (solar weighted)	0.027	0.016

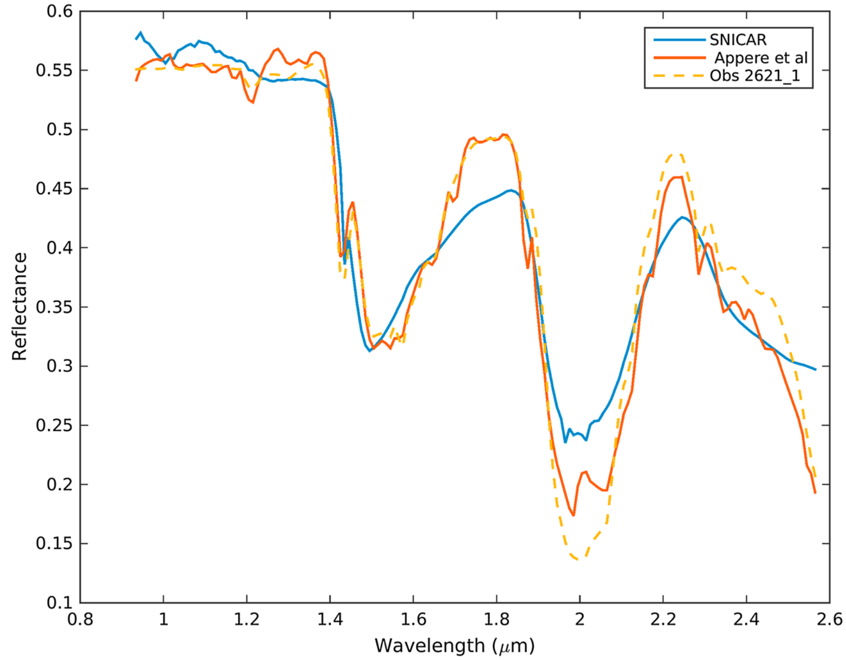

Figure 17. Comparison of best fit albedo by using SNICAR and the model applied by *Appéré et al.* [2011] against data from OMEGA observation 2621_1.

5. Conclusions

We have simulated the spectral albedo of CO_2 snow by using an enhanced 480-band version of SNICAR, which was previously developed for terrestrial snow. We explored CO_2 snow albedo across the entire solar spectrum, including UV, visible, and near-IR wavelengths. Our analysis shows significant differences between H_2O and CO_2 snow albedos. H_2O snow is about 8 times more absorptive than CO_2 snow in the near-IR region and 7 times more absorptive averaged over the entire solar spectrum. CO_2 snow albedo shows very little dependence on solar zenith angle and a weaker dependence on grain size than H_2O snow. The broadband albedo of CO_2 snow decreases by only 0.064 as effective grain size increases from 50 to 1500 μm.

The presence of thin snow layers exposes underlying surfaces to incoming radiation, hence impacting the surface albedo. The saturation thicknesses for CO_2 snow and H_2O snow range from approximately 6.5–100 cm and 5–83 cm, respectively, for effective grain sizes ranging from 50 to 1500 μm, though we caution again that these thicknesses may be smaller with nonspherical ice particles. Nonspherical grains scatter less strongly in the forward direction, thereby decreasing the penetration depth of solar radiation. Thicker CO_2 snow is required to negate the impact of underlying surface because CO_2 ice grains scatter more strongly than H_2O ice grains, especially in the near-IR spectrum. The presence of 0.01% dust reduces the broadband albedo of CO_2 snow by about 50%, with Martian dust being the darkest type of dust explored here, followed by typical Earth dust and palagonite. The spectral shape of albedo changes caused by palagonite, which is often used as a Martian dust analog, closely follow those of Mars dust, but palagonite is not as absorptive as Mars dust. The impact of dust on CO_2 snow albedo saturates after its mass mixing ratio exceeds roughly 0.1%.

Because of the contrasting properties of H_2O and CO_2 ice in the near-IR spectrum, different layering and mixing configurations of these types of snow can have substantial impact on net surface albedo. With an effective grain size of 100 μm, only about 2.5 cm of H_2O snow is needed to mask the influence of underlying CO_2 snow on net surface albedo (Table 5), while more than double of this amount of CO_2 snow is needed to mask the influence of H_2O snow (Table 6). Such effects are relevant for the perennial H_2O ice caps of Mars, and where water vapor from the atmosphere condenses on top of CO_2 ice in other areas of the planet. When both snow types are present as a mixture rather than separate layers, 0.01% of H_2O snow reduces the broadband albedo of CO_2 snow by 0.03, while 1% of CO_2 snow is required to increase the broadband albedo of H_2O snow by the same amount.

With the identification of optimal snow parameter combinations, our results show a decent agreement between modeled spectral albedo and observed reflectance of the Martian polar ice caps in the 1–4 μm spectral range. The CRISM data exhibit anomalously high reflectance at 2.7 μm, which cannot be explained with the presence of either CO_2 or H_2O ice, as both media are highly absorptive at this wavelength. SNICAR also provides realistic best fit parameters for matching OMEGA near-IR observations, though the spectral fit is not as good as that achieved previously with a directional reflectance model [*Appéré et al.*, 2011]. Simulations presented here could potentially be used in combination with observed data to refine the calibration of surface albedo retrieval algorithms. Model results can also be used to interpolate measurements to higher spectral resolution. The new spectrally resolved albedos for CO_2 snow presented here have potentially wide applicability to any planet or system with CO_2 ice, especially Mars.

Acknowledgments
We are grateful to Michael Mischna, Mike Wolff, Jeffrey Johnson, Adrian Brown, and Thomas Appéré for providing, respectively, CO_2 ice refractive indices derived from Gary Hansen's measurements, Martian dust optical properties, palagonite optical properties, surface reflectivity derived from CRISM observations, and observed and modeled albedo derived from OMEGA observations. A single-layer implementation of SNICAR can be operated interactively on the Web at http://snow.engin.umich.edu. This work was partially supported by NASA NNX13AN29G and NSF ARC-1253154.

References

Appéré, T., B. Schmitt, Y. Langevin, S. Douté, A. Pommerol, F. Forget, A. Spiga, B. Gondet, and J.-P. Bibring (2011), Winter and spring evolution of northern seasonal deposits on Mars from OMEGA on Mars Express, *J. Geophys. Res.*, *116*, E05001, doi:10.1029/2010JE003762.

Balkanski, Y., M. Schulz, T. Claquin, and S. Guibert (2007), Reevaluation of mineral aerosol radiative forcings suggests a better agreement with satellite and AERONET data, *Atmos. Chem. Phys.*, *7*(1), 81–95.

Banin, A., F. X. Han, I. Kan, and A. Cicelsky (1997), Acidic volatiles and the Mars soil, *J. Geophys. Res.*, *102*, 13,341–13,356, doi:10.1029/97JE01160.

Barr, A. C., and S. M. Milkovich (2008), Ice grain size and the rheology of the martian polar deposits, *Icarus*, *194*(2), 513–518, doi:10.1016/j.icarus.2007.11.018.

Bell, J. F., III (1996), Iron, sulfate, carbonate, and hydrated minerals on Mars, in *Mineral Spectroscopy: A Tribute to Roger G. Burns*, *Spec. Publ.*, vol. 5, edited by M. D. Dyar, C. McCammon, and M. W. Schaefer, pp. 359–380, Geochem. Soc, London.

Bell, J. F., III, T. B. McCord, and P. D. Owensby (1990), Observational evidence of crystalline iron oxides on Mars, *J. Geophys. Res.*, *95*, 14,447–14,461, doi:10.1029/JB095iB09p14447.

Bibring, J. P., et al. (2004), Perennial water ice identified in the south polar cap of Mars, *Nature*, *428*(6983), 627–630.

Bibring, J. P., et al. (2005), Mars surface diversity as revealed by the OMEGA/Mars Express observations, *Science*, *307*(5715), 1576–1581.

Bonev, B. P., G. B. Hansen, D. A. Glenar, P. B. James, and J. E. Bjorkman (2008), Albedo models for the residual south polar cap on Mars: Implications for the stability of the cap under near-perihelion global dust storm conditions, *Planet. Space Sci.*, *56*(2), 181–193, doi:10.1016/j.pss.2007.08.003.

Brown, A. J., W. M. Calvin, P. C. McGuire, and S. L. Murchie (2010), Compact Reconnaissance Imaging Spectrometer for Mars (CRISM) south polar mapping: First Mars year of observations, *J. Geophys. Res.*, *115*, E00D13, doi:10.1029/2009JE003333.

Brown, A. J., W. M. Calvin, and S. L. Murchie (2012), Compact Reconnaissance Imaging Spectrometer for Mars (CRISM) north polar springtime recession mapping: First 3 Mars years of observations, *J. Geophys. Res.*, *117*, E00J20, doi:10.1029/2012JE004113.

Brown, A. J., S. Piqueux, and T. N. Titus (2014), Interannual observations and quantification of summertime H_2O ice deposition on the Martian CO_2 ice south polar cap, *Earth Planet. Sci. Lett.*, *406*, 102–109.

Byrne, S., M. T. Zuber, and G. A. Neumann (2008), Interannual and seasonal behavior of Martian residual ice-cap albedo, *Planet. Space Sci.*, *56*(2), 194–211.

Christensen, P. R., et al. (2000), Detection of crystalline hematite mineralization on Mars by the Thermal Emission Spectrometer: Evidence for near-surface water, *J. Geophys. Res.*, *105*, 9623–9642, doi:10.1029/1999JE001093.

Christensen, P. R., et al. (2001a), Mars Global Surveyor Thermal Emission Spectrometer experiment: Investigation description and surface science results, *J. Geophys. Res.*, *106*, 23,823–23,871, doi:10.1029/2000JE001370.

Christensen, P. R., R. V. Morris, M. D. Lane, J. L. Bandfield, and M. C. Malin (2001b), Global mapping of Martian hematite mineral deposits: Remnants of water-driven processes on early Mars, *J. Geophys. Res.*, *106*, 23,873–23,885, doi:10.1029/2000JE001415.

Clancy, R. T., S. W. Lee, G. R. Gladstone, W. W. McMillan, and T. Roush (1995), A new model for Mars atmospheric dust based upon analysis of ultraviolet through infrared observations from Mariner 9, Viking, and Phobos, *J. Geophys. Res.*, *100*, 5251–5264, doi:10.1029/94JE01885.

Clark, R. N., T. V. King, M. Klejwa, G. A. Swayze, and N. Vergo (1990), High spectral resolution reflectance spectroscopy of minerals, *J. Geophys. Res.*, *95*, 12,653–12,680, doi:10.1029/JB095iB08p12653.

Douté, S., and B. Schmitt (1998), A multilayer bidirectional reflectance model for the analysis of planetary surface hyperspectral images at visible and near-infrared wavelengths, *J. Geophys. Res.*, *103*, 31,367–31,389, doi:10.1029/98JE01894.

Egan, W. G., and F. A. Spagnolo (1969), Complex index of refraction of bulk solid carbon dioxide, *Appl. Opt.*, *8*(11), 2359–2360, doi:10.1364/AO.8.002359.

European Committee for Standardization (2003), *EN 1991-1- 1: Eurocode 1 – Actions on Structures – Part 1–3: General Actions – Snow Loads*, Eur. Comm. for Stand., Brussels.

Flanner, M. G., C. S. Zender, J. T. Randerson, and P. J. Rasch (2007), Present day climate forcing and response from black carbon in snow, *J. Geophys. Res.*, *112*, D11202, doi:10.1029/2006JD008003.

Flanner, M. G., C. S. Zender, P. G. Hess, N. M. Mahowald, T. H. Painter, V. Ramanathan, and P. J. Rasch (2009), Springtime warming and reduced snow cover from carbonaceous particles, *Atmos. Chem. Phys.*, *9*, 2481–2497.

Forget, F. (1998), Mars CO_2 ice polar caps, in *Solar System Ices*, pp. 477–507, Springer, Dordrecht, Netherlands, doi:10.1007/978-94-011-5252-5.

Forget, F., F. Hourdin, and O. Talagrand (1998), CO_2 snowfall on Mars: Simulation with a general circulation model, *Icarus*, *131*(2), 302–316.

Fu, Q. (2007), A new parameterization of an asymmetry factor of cirrus clouds for climate models, *J. Clim.*, *64*, 4140–4150, doi:10.1175/2007JAS2289.1.

Hansen, G. B. (1997), The infrared absorption spectrum of carbon dioxide ice from 1.8 to 333 μm, *J. Geophys. Res.*, *102*, 21,569–21,587, doi:10.1029/97JE01875.

Hansen, G. B. (1999), Control of the radiative behavior of the Martian polar caps by surface CO_2 ice: Evidence from Mars Global Surveyor measurements, *J. Geophys. Res.*, *104*, 16,471–16,486, doi:10.1029/1998JE000626.

Hansen, G. B. (2005), Ultraviolet to near-infrared absorption spectrum of carbon dioxide ice from 0.174 to 1.8 μm, *J. Geophys. Res.*, *110*, E11003, doi:10.1029/2005JE002531.

Hansen, J. E., and L. D. Travis (1974), Light scattering in planetary atmospheres, *Space Sci. Rev.*, *16*(4), 527–610.
Herr, K. C., and G. C. Pimentel (1969), Infrared absorptions near three microns recorded over the polar cap of Mars, *Science*, *166*(3904), 496–499.
Kieffer, H. H., and T. N. Titus (2001), TES mapping of Mars' north seasonal cap, *Icarus*, *154*(1), 162–180.
Kieffer, H. H., T. N. Titus, K. F. Mullins, and P. R. Christensen (2000), Mars south polar spring and summer behavior observed by TES: Seasonal cap evolution controlled by frost grain size, *J. Geophys. Res.*, *105*, 9653–9699, doi:10.1029/1999JE001136.
Labs, D., and H. Neckel (1968), The radiation of the solar photosphere from 2000 Å to 100 μm, *Z. Astrophys.*, *69*, 1.
Langevin, Y., J.-P. Bibring, F. Montmessin, F. Forget, M. Vincendon, S. Douté, F. Poulet, and B. Gondet (2007), Observations of the south seasonal cap of Mars during recession in 2004–2006 by the OMEGA visible/near-infrared imaging spectrometer on board Mars Express, *J. Geophys. Res.*, *112*, E08S12, doi:10.1029/2006JE002841.
Larson, H. P., and U. Fink (1972), Identification of carbon dioxide frost on the Martian polar caps, *Astrophys. J.*, *171*, L91.
Leighton, R. B., and B. C. Murray (1966), Behavior of carbon dioxide and other volatiles on Mars, *Science*, *153*(3732), 136–144.
Libois, Q., G. Picard, J. L. France, L. Arnaud, M. Dumont, C. M. Carmagnola, and M. D. King (2013), Influence of grain shape on light penetration in snow, *Cryosphere*, *7*, 1803–1818, doi:10.5194/tc-7-1803-2013.
Montmessin, F., and F. Lefèvre (2013), Transport-driven formation of a polar ozone layer on Mars, *Nat. Geosci.*, *6*(11), 930–933, doi:10.1038/ngeo1957.
Räisänen, P., A. Kokhanovsky, G. Guyot, O. Jourdan, and T. Nousiainen (2015), Parameterization of single-scattering properties of snow, *Cryosphere*, *9*, 1277–1301, doi:10.5194/tc-9-1277-2015.
Sokolik, I. N., and O. B. Toon (1999), Incorporation of mineralogical composition into models of the radiative properties of mineral aerosol from UV to IR wavelengths, *J. Geophys. Res.*, *104*, 9423–9444, doi:10.1029/1998JD200048.
Stroncik, N. A., and H. U. Schmincke (2002), Palagonite—A review, *Int. J. Earth Sci.*, *91*(4), 680–697.
Tillman, J. E., N. C. Johnson, P. Guttorp, and D. B. Percival (1993), The martian annual atmospheric pressure cycle: Years without great dust storms, *J. Geophys. Res.*, *98*, 10,963–10,971, doi:10.1029/93JE01084.
Toon, O. B., C. P. McKay, T. P. Ackerman, and K. Santhanam (1989), Rapid calculation of radiative heating rates and photodissociation rates in inhomogeneous multiple scattering atmospheres, *J. Geophys. Res.*, *94*, 16,287–16,301, doi:10.1029/JD094iD13p16287.
Warren, S. G., and R. E. Brandt (2008), Optical constants of ice from the ultraviolet to the microwave: A revised compilation, *J. Geophys. Res.*, *113*, D14220, doi:10.1029/2007JD009744.
Warren, S. G., W. J. Wiscombe, and J. F. Firestone (1990), Spectral albedo and emissivity of CO_2 in Martian polar caps: Model results, *J. Geophys. Res.*, *95*, 14,717–14,741, doi:10.1029/JB095iB09p14717.
Wiscombe, W. J., and S. G. Warren (1980), A model for the spectral albedo of snow. I: Pure snow, *J. Atmos. Sci.*, *37*, 2712–2733, doi:10.1175/1520-0469(1980)037<2712:AMFTSA>2.0.CO;2.
Wolff, M. J., et al. (2006), Constraints on dust aerosols from the Mars Exploration Rovers using MGS overflights and Mini-TES, *J. Geophys. Res.*, *111*, E12S17, doi:10.1029/2006JE002786.
Wolff, M. J., M. D. Smith, R. T. Clancy, R. Arvidson, M. Kahre, F. Seelos IV, S. Murchie, and H. Savijarvi (2009), Wavelength dependence of dust aerosol single scattering albedo as observed by the Compact Reconnaissance Imaging Spectrometer, *J. Geophys. Res.*, *114*, E00D04, doi:10.1029/2009JE003350.
Wolff, M. J., R. T. Clancy, J. D. Goguen, M. C. Malin, and B. A. Cantor (2010), Ultraviolet dust aerosol properties as observed by MARCI, *Icarus*, *208*(1), 143–155.